Self-consistent dynamical mean-field investigation of exotic structures in isospin-asymetric nuclear matter

F. Sébille, S. Figerou, V. de La Mota

Self-consistent dynamical mean-field investigation of exotic structures in isospin-asymmetric nuclear matter

F. Sébille, S. Figerou and V. de la Mota

SUBATECH, Ecole des Mines, Université de Nantes, CNRS/IN2P3, Nantes, France

Abstract

The exotic structures expected in the outermost layer of neutron stars are investigated in a new approach. It is based on the DYnamical WAvelets in Nuclei (DYWAN) model of nuclear collisions. This microscopic dynamical approach is an Extended Time-Dependent Hartree-Fock description based on a wavelet representation. The model addresses the dynamical exploration of complex nuclear structures, beyond the Wigner-Seitz (WS) approximation and without any assumption on their final shapes. The present study focuses on exotic phases of cold matter evidenced dynamically at sub-saturation densities, currently within a pure mean field framework, before tackling the effects of the multi-particle correlations in a forthcoming study. Starting from inhomogeneous initial conditions provided by nuclei located on an initial crystalline lattice, the exotic structures result from a dynamical self-consistent treatment where, in principle, the nuclear system can freely self-organize, modify the lattice structure or even break the lattice and the initial matter distribution symmetries. In this work nuclei are initially slightly excited with low-lying collective modes. The system can then explore geometrical configurations with similar energies, without being trapped in the vicinity of a local minimum. In this quantum framework, different effects are analyzed, among them the sensitivity to the Equation of State and to the proton fraction.

1 Introduction

Neutron stars have fascinated physicists since their prediction [1] in the early years of the XXth century. They have been conceived as the remnant, composed of essentially densely-packed neutrons, which is left behind the explosion of a massive star. A considerable effort has been done by different theoretical models in order to understand the properties of this extreme state of matter and to describe the observed phenomena. The mechanisms involved in the build up of a neutron star from the explosion of a supernova is not yet well understood and constitutes an active field of research [2] [3].

Theoretical models agree in the fact that after the formation of the neutron star its temperature is around 10 MeV and falls rapidly compared with its life-time to 0.1 MeV [4]. It is usual to divide the neutron star into three different density regions [3]. The outermost layer, which has been extensively studied, extends up to around 10^{11} g/cm^3 and is supposed to be composed of essentially a crystalline lattice of neutron-rich nuclei immersed in a degenerate electron gas. The second region extends from there up to a density of nearly 10^{14} g/cm^3 and in addition to the neutron-rich nuclei it is composed by both degenerate electron and neutron gases. In the last region, at still higher densities the matter consists of a uniform liquid of neutrons, protons and electrons and other elementary particles start to appear as density increases. For a review we refer the reader to Ref. [5].

We will focus ourselves on the study of the crust, which corresponds to roughly the two first mentioned regions. In this range of densities, matter may be correctly described in terms of interacting nucleons, while at higher densities other degrees of freedom will play an important role. Even if the crust region is relatively thin (less than 10% of the radius) it constitutes the interface between the star and the observer, in consequence the knowledge of the properties of the outer parts of the star is important for the understanding of different internal phenomena .

In this region the existence of nuclei with exotic shapes has been predicted independently by Refs. [6] and [7] both based on a liquid-drop description. These structures, referred to as "pasta" phases, are expected to occur at sub-nuclear densities. They are the result of the delicate interplay between Coulomb and nuclear forces [6, 7, 8, 9]. The appearance of these phases may have important astrophysical consequences. Their presence are expected to influence the cooling process of the

neutron star and can modify the interaction between matter and neutrinos [10, 11]. The pioneer prediction of pasta phases has been confirmed by other models. Among them let us mention the works in the domain of the Thomas-Fermi (TF) theory [12, 13, 14], or in the extended-TF approach [15], those in the framework of the Compressible Liquid-Drop model [16, 17, 18], those in Molecular Dynamics (MD) approaches [10, 11, 19], those in self-consistent Hartree-Fock (HF) models [20]-[24] and those in Relativistic Mean field approaches [25, 26]. Thermodynamical properties of the crust matter have been studied by these models. In TF and in liquid-drop models, the different structural phases are prepared and equilibrium conditions determined through energy considerations. In several works, there are also attempts to address the formation of exotic structures without assuming possible shapes or symmetries [27, 25].

In this work we present a new dynamical approach, the DYWAN model, to investigate the expected development of complex structures with many possible nuclear shapes in neutron star crust. These structures are related to the existence of a large number of low-energy configurations. Different frameworks could examine these configurations, among which simulated annealing type techniques. Nevertheless, in the present work we are interested in a dynamical exploration of these multiple low-lying energy minima. Therefore, concerning the neutron star crust properties the induced excitations are not realistic but rather they are probes of matter configurations. The final objective will be to address the question of structural configurations both beyond a mean-field approximation and the Wigner-Seitz approximation. But before tackling these aspects and keeping in mind that at low-energy excitations a leading contribution is provided by the mean-field, the aim of this work is two folded. On hand we will investigate the role of a pure mean field at zero temperature. On the other hand we will check the accessible numerical accuracy in order to be able in future simulations to disentangle physical fluctuations from numerical ones. Furthermore, a main goal is to let the nuclear system freely self-organize in a given region (super-cell) of space as large as possible. Wigner-Seitz cells are used to prepare initial conditions with initial lattices, later on in the evolution, the numerical treatment will be able to modify the lattice structure, or to break the lattice and initial matter distribution symmetries. The only constraint kept during the dynamics is the periodic boundary conditions on the super-cell, those on WS cells having been completely released. Nuclei and simple cubic lattices currently define the initial seed of the self-consistent treatment, but only the final results are relevant in the discussion of neutron star crust configurations. Concerning the mean field evolu-

tion, and from a numerical point of view, the present starting conditions provide the most compelling constraints. Indeed, from simple cubic lattice the system can be driven to meta-stable equilibrium since other lattices, like body centred lattices, are expected to be more stable. These meta-stable equilibrium states are very sensitive and can be quickly destroyed by numerical inaccuracies. The fact that they survive over time periods longer than some thousands Fm/c evidences the efficiency of the mean-field treatment. Forthcoming investigations relevant to neutron star crusts, will include the sensitivity to the initial inputs of the self-consistent treatment (like nuclei species, heterogeneities, crystal lattice structures, and scaling laws) as well as to collective, thermal excitations and fluctuations.

This work is organized as follows. In Section 2 we present the basis of our theoretical approach, where the initial conditions, the static properties and the dynamical evolution of the system are described. In Section 3 we present the numerical treatment of the Coulomb interaction. In Section 4 the morphological analysis techniques applied to the structures are briefly described. In Section 5 the results of the dynamical investigation of structure formation are presented and discussed. Finally our conclusions are given in Section 6.

2   The model

We have recently developed a model which describes the behaviour of the nuclear matter at sub-nuclear densities and low temperatures characterizing the crust of a neutron star. It has been built in the framework of the DYWAN model [28] which was proven to correctly reproduce the main features of nuclear reactions [28, 29, 30]. The DYWAN model, based on the principles of projection methods [31], is given in terms of the projection of the complete density operator onto the subspace associated with the available information. In this sense, a hierarchy of approximations can be built according to the level of complexity of the description. Concerning the nuclear dynamics at intermediate energies, these different levels are connected with the treatment of multi-particle correlations. At the lowest level, the description is given by the projection of the space of states onto the one-body subspace, neglecting all couplings with other degrees of freedom. This is the Time-Dependent Hartree-Fock (TDHF) approximation where the dynamics is completely ruled by the mean-field, without particle correlations others than averaged two-body ones. In a second level stands the Extended-TDHF description, where a coupling with two-particle correla-

tions is kept in order to include dissipative effects. At this level, the mean-field [32] is still playing a preponderant role. Going beyond the ETDHF level would need to introduce higher order particle correlations, to complete the description of density fluctuations and the dispersions of dynamical observables. Nevertheless, the number of degrees of freedom is so high that the problem becomes intractable. In a previous work [30] we proposed a simplified procedure for the treatment of dynamical multiparticle correlations according to a random phase approximation.

In this work we will remain at the lowest level of the mentioned hierarchy of approximations since we are mainly interested in the study of the mean-field influence on a cold nuclear system. As a matter of fact, it has been shown [20] that if the temperature of the star is below 10^8 K and the density below 2.8×10^{14} g/cm^3, the conditions for the validity of mean-field theories are satisfied. At neutron star densities and temperatures nuclear matter can be modeled by a neutral mixture of nuclei, electrons and, eventually, free neutrons. Nuclei are expected to form a crystalline lattice and electrons are considered as a degenerate relativistic gas [3, 33]. In our approach electrons are modelled by a uniform charge density background in which nuclei are immersed, and which ensures the neutrality of the system.

The general structure of the model is the following: first of all a static Hartree-Fock (HF) self-consistent procedure is implemented in order to get nuclear composites either at their ground states or in excited states induced according to mechanical or thermal constraints. These nuclei are used to construct the initial nuclear lattice surrounded by the degenerate electron gas. Afterwards, nuclei are led to evolve according to TDHF-type equations of motion, allowing the crust matter to self-organize in a dynamical way. Accordingly, our description can be separated into two main parts, one of them concerning the preparation of initial state of the system, the other one concerning its subsequent evolution. These aspects will be presented separately in the following Sections.

2.1   Initial configuration

The solid phase of the outermost layer of a neutron star is assumed to be composed by an orderly arrangement of neutron rich nuclei in a crystal-like structure. An initial guess of such a solid crystal can be constructed from a three-dimensional lattice with periodic boundary conditions. This lattice is built by stacking up a cubic

super-cell in three spatial directions. The characteristics of this cell, as the length and the type (simple cubic, body centred, face centred) can be arbitrarily chosen. The super-cell is composed by a fixed number of WS cells (see Fig. 1) in which single nuclei are self-consistently prepared, beyond the WS approximation [34]. These initial conditions, by construction, involve implicitly periodic boundary conditions for the WS cells. During the subsequent dynamical self-consistent evolution, the periodic boundary conditions are only strictly imposed to the super-cell all along the calculation, without Bloch periodic boundary conditions [35] on the WS cells.

In the WS cell the HF equation for each nucleus is solved as follows. An iterative procedure is implemented to work out the single particle (s.p.) eigenvalue equations $h|\varphi_n >= \epsilon_n|\varphi_n >$, the one-body hamiltonian h taking the following form:

$$h = -\frac{\hbar^2}{2m}\Delta + V^{HF}$$

We have chosen a density-dependent zero-range effective interaction, of the Zamick type [36], with the following self-consistent field:

$$\begin{aligned}
V_q^{HF}(\rho,\xi) &= \frac{t_0'}{\rho_\infty}\rho + \frac{t_3'}{\rho_\infty^{\nu+1}}\rho^{\nu+1} + \frac{c}{\rho_\infty^2}\xi^2 + \frac{4qc}{\rho_\infty^2}\rho\xi + \\
&\quad \frac{\Omega}{3\rho_\infty^2}\xi^2 + \frac{4q\Omega}{3\rho_\infty^2}(\rho - \rho_\infty)\xi + V_q^C \\
\text{with}: \quad \rho &= \rho_n + \rho_p \\
\xi &= \rho_n - \rho_p
\end{aligned} \tag{1}$$

where ρ_n and ρ_p stand for neutron and proton densities, $q=1/2$ for neutrons and $-1/2$ for protons, and $\rho_\infty=0.145$ fm^{-3} is the saturation density of infinite nuclear matter [37].

If we call t_0, t_3, x_0 and x_3 the usual Skyrme effective interaction parameters [38] we have the following relationships: $t_0' = \frac{3\rho_\infty}{4}t_0$ and $t_3' = \frac{3(\nu+2)\rho_\infty^{\nu+1}}{48}t_3$ with $x_0 = x_3 = -1/2$. In Eq. (1) V_q^C, the Coulomb potential associated with the proton distribution, has been calculated in the initial state within a Haar wavelet approximation. The spin-orbit term was not included in this first version, as well as the momentum-dependent contributions. These terms deserve further investigations since their influence is the matter of active research and different interpretations [22, 32, 39]. In Table 1 we present the coefficients of the force for two different values of the compressibility modulus: $K_\infty= 200$ MeV and 380 MeV for the soft and hard equations of state (EOS), respectively.
The current values of c and Ω were chosen in order to reproduce the typical values of baryon density energies in infinite matter [40]. They are initially fixed at $c=20$ MeV
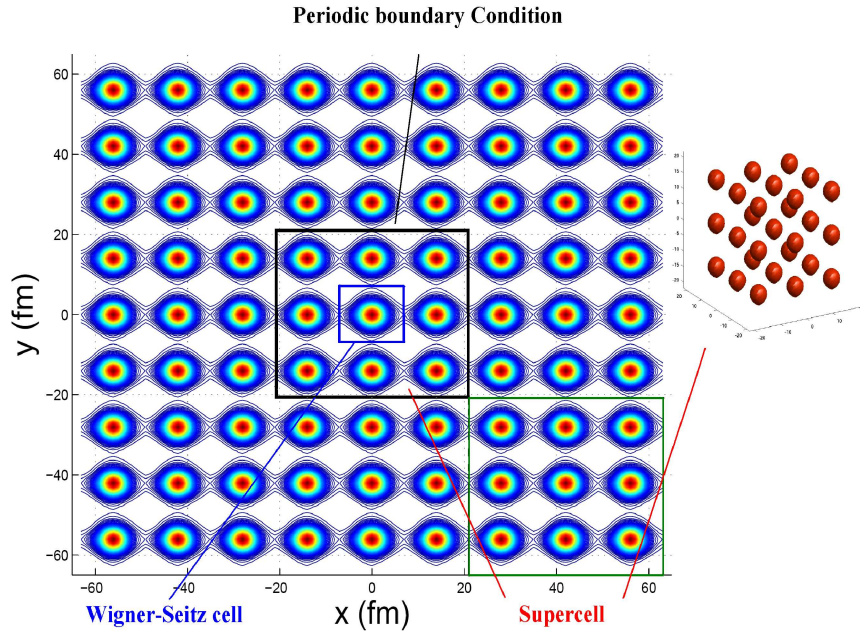
6

Figure 1: Density profiles of an initial crystal lattice. The Wigner-Seitz cell is displayed as well as the supercell where the matter can freely self-organize. Infinite matter is simulated by periodic boundary conditions.

Table 1: Parameters of the local Zamick interaction

	t'_0/ρ_∞(MeV fm^3)	$t'_3/\rho_\infty^{\nu+1}$(MeV fm$^{3(\nu+1)}$)	ν
Soft	-356	303	1/6
Hard	-123	70	1

and Ω=-100 MeV. The principal static characteristics of nuclei, as binding energies, radii and equilibrium densities are correctly reproduced with this simplified force. They constitute a good approximation even in the case where the isospin-dependent part of the potential is neglected [28, 29, 30]. As stated in recent works [41], EOS parameters are still uncertain because they are not completely constrained from nuclear data, then a study of their influence on the overall dynamics seems necessary.

At each iteration the different s.p. energy levels, for each value of q, are calculated according to a potential well discretization on a 3-dimensional lattice. The step of the lattice is typically of 0.5 fm. According to the numerical resolution scheme of the DYWAN model describing nuclear collisions the corresponding s.p. wave-functions

are expanded in an orthogonal wavelet basis $\{|\psi_i^\lambda>\}$:

$$|\varphi_\lambda >= \sum_i \omega_i^\lambda |\psi_i^\lambda > \tag{2}$$

where ω_i^λ are their corresponding weights. Wavelets are non-stationary wave functions from which Hilbert space bases can be built up. A family of wavelets is constructed by translating and expanding the generating function, called mother wavelet:

$$\psi_{a,b}(x) = \frac{1}{\sqrt{a}}\psi(\frac{x-b}{a})$$

where a and b are, respectively, the compression and translation parameters. At a given scale, any signal can be analyzed in terms of these functions in an optimal way for a convenient choice of a discrete basis which relies on entropy criteria.

Among the different families of wavelets we have favored in (2) spline bases [42] which either are compactly supported or respect the symmetries of the analyzed s.p. functions. Even if splines are not analytic functions, they can be accurately approximated by a linear combination of analytic functions. For physical convenience and interpretation, wavelets are split in progressive and regressive wavelets through Hilbert transforms. These progressive wavelets are generalized coherent states which can be efficiently fitted by Gabor generalized coherent states as emphasized in [43]. These coherent states are complex valued functions having the following form :

$$\alpha_i(x) = \mathcal{N}_i \mathrm{e}^{-\gamma_1(x-<x>_i)^2} e^{-\gamma_2(x-<x>_i)} \tag{3}$$

Here, $\mathcal{N}_i$ is a normalization factor and the complex coefficients γ_1 and γ_2 are related to the first and second moments in configuration and momentum space (see Ref. [28]):

$$< x >= \xi_x \quad < (x-\xi_x)^2 >= \chi_x \quad < p_x >= \pi_x \quad < (p_x-\pi_x)^2 >= \phi_x$$

$$\sigma =< \frac{1}{2}[(x-\xi_x),(p_x-\pi_x)]_+ >$$

where $[\ ,\ ]_+$ represents the anticommutation operation. The momentum-position correlation σ satisfies the generalized uncertainty relationship:

$$\Delta = \chi\phi - \sigma^2 = \frac{\hbar^2}{4} \tag{4}$$

Similar expressions can be written for y and z components. The preceding analysis provides for each s.p. level an ensemble of 12 correlated coordinates $\{\vec{\xi}, \vec{\chi}, \vec{\pi}, \vec{\phi}\}$ representing the centroids and widths of wavelets in phase space.

8

The one-body density matrix $\rho = \sum_{\lambda=0}^{N} |\varphi_\lambda> <\varphi_\lambda|$ can be then written in terms of wavelets in the following way:

$$\rho = \sum_{\lambda=0}^{N} \sum_{i,j} \beta_{i,j}^\lambda |\alpha_i^\lambda> <\alpha_j^\lambda| \qquad (5)$$

where $\beta_{i,j}^\lambda = \omega_i^\lambda \omega_j^{\lambda\star}$. Following Ref. [28], where the role of the different contributions to ρ has been discussed, only the diagonal terms will contribute efficiently to mean-field evaluation, since they provide the relevant information to our (mean-field) description. As a matter of fact, the off-diagonal terms are shown to oscillate very rapidly and interfere destructively providing vanishing mean values. An analytical phase space representation of a progressive wavelet contribution to the one body density matrix is given by the Wigner transform of the analytical fit mentioned in Eq. (3):

$$\alpha^w(x,p) = \frac{1}{2\pi\sqrt{\Delta}} \; e^{-\frac{1}{2\Delta}(\phi(x-<x>)^2 + \chi(p-<p>)^2 - 2\sigma(x-<x>)(p-<p>))} \qquad (6)$$

Once the one body density matrix ρ and the corresponding one-body potential V_q^{HF} are calculated the iterative process proceeds until the convergence of the Fermi energy level is reached. The W.S. nucleus can also be prepared initially in a slightly excited state with a given deformation or at a finite temperature.

2.2 Nuclear matter behaviour at sub-nuclear densities

We proceed to show the results in equilibrium nuclear matter configuration at zero temperature extracted from the DYWAN model. The properties of matter at sub-nuclear densities are affected by the behaviour of nuclei resulting from the nuclear interaction and it is important to check whether the effective nuclear force given by Eq. (1) yields realistic values of these quantities. As pointed out by other authors [41, 44], one of the principal physical quantities reflecting the characteristics of the force is the energy per baryon of pure neutron matter. This quantity is defined as:

$$\omega = \frac{\varepsilon}{\rho} = \frac{\int V_q^{HF} \, d\rho}{\rho} + \omega_{kin}$$

where ω_{kin} is the corresponding kinetic contribution. If V_q^{HF} is given by Eq. (1)

then ω takes the following form :

$$\omega(\rho, \delta) \;=\; \frac{t_0'}{2\rho_\infty}\,\rho \;+\; \frac{t_3'}{((\nu+2)\rho_\infty^{\nu+1}}\,\rho^{\nu+1} \;+\; \frac{c}{\rho_\infty^{\,2}}\delta^2\rho^2 \tag{7}$$

$$+\; \frac{\Omega}{3\rho_\infty^{\,2}}(\rho - \rho_\infty)\rho\delta^2 + \omega_{kin}$$

$$\text{with} \quad \delta \;=\; (\rho_n - \rho_p)/\rho$$

Calculated in uniform matter, ω_{kin} leads to an analytic formulation depending on the density ρ and on the asymmetry δ as follows:

$$\omega_{kin} = \frac{\hbar^2}{2m}\frac{3}{5}(3\pi^2)^{2/3}\rho^{2/3}\left[\left(\frac{1-\delta}{2}\right)^{\frac{5}{3}} + \left(\frac{1+\delta}{2}\right)^{\frac{5}{3}}\right] \tag{8}$$
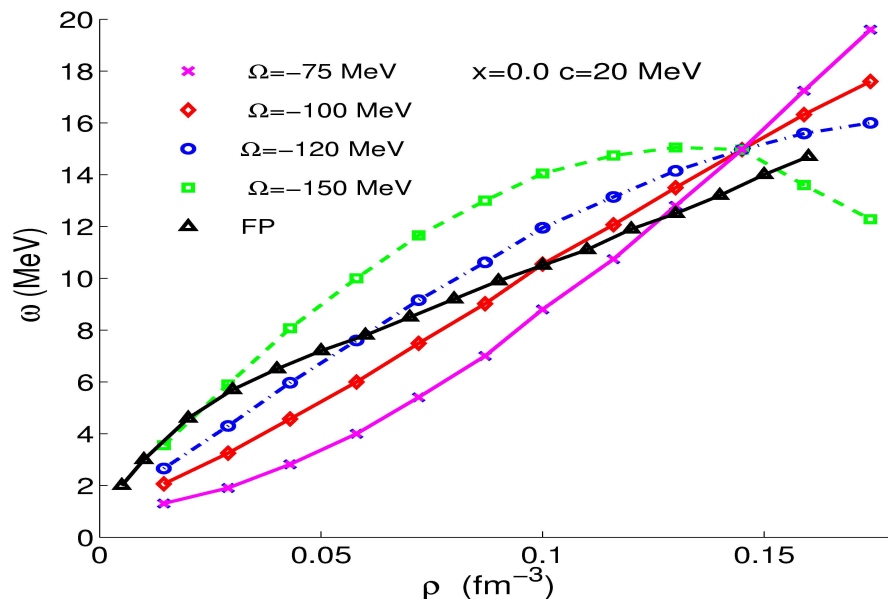

Figure 2: Energy density per baryon in cold neutron matter as a function of the density at different values of the asymmetry parameter Ω. The results of Ref. [40] are in triangles.

In Fig. 2 we represent the values of $\omega(\rho)$ in pure neutron matter for different values of the asymmetry constant Ω and with c=20 MeV. Together with these values are plotted the results of Ref. [40] in triangles. In all these cases the constant c has been fixed in order to obtain similar values of ω in pure neutron matter to those of Ref. [40] when, in each case, the densities reach their respective saturation values in symmetric nuclear matter. We observe a global agreement between both calculations
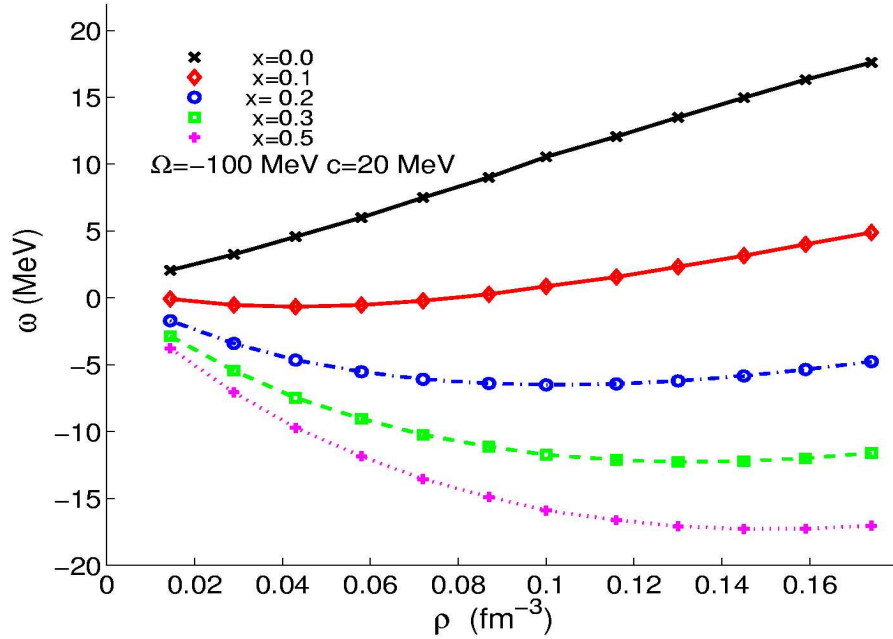
Figure 3: Energy density per baryon in cold nuclear matter as a function of the density at different proton fractions.

for the given set of Ω values. This fact is extremely interesting considering the simplicity of the implemented effective force.

In Fig. (3) we represent the values of $\omega(\rho, \delta)$ at zero temperature for asymmetric nuclear matter at different proton fractions x. The parameters Ω and c have been fixed at 100 and 20 MeV, respectively. In our approach we have determined phenomenologically the density dependence of the symmetry energy according to its current estimate at the saturation value in pure neutron matter. This differs from other models [45, 46, 23] where several complex requirements have been imposed on the energy per baryon, at different proton fractions, and on different physical quantities related with its derivatives. In fact, the scope of this work was not to perform an exhaustive study of the equilibrium properties of nuclear matter. We rather looked to establish the bases of the present model describing the dynamical behaviour of nuclear matter at sub-nuclear densities. In this case a simple effective force has been implemented, but in future calculations more sophisticated forces will be introduced. Recent improvements in the treatment of the EOS have been done, in particular in astrophysical applications [47, 48] .

Other physical quantities of interest in the characterization of the effective inter-

action are nucleon chemical potentials:

$$\mu_i = \frac{\partial \varepsilon}{\partial \rho_i} \qquad i = n, p.$$

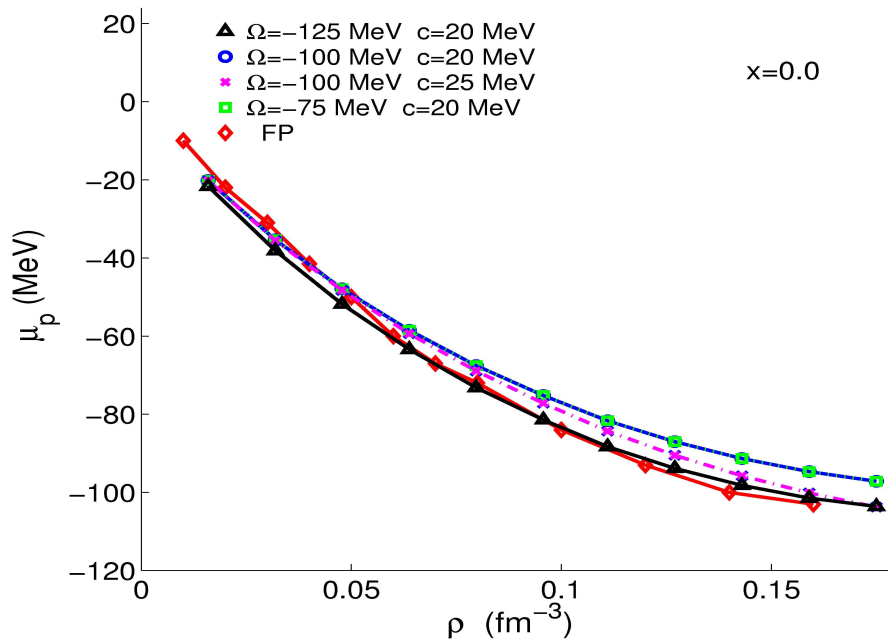In Fig. (4) is depicted the neutron density dependence of the proton chemical

Figure 4: Proton chemical potential in cold neutron matter as a function of the neutron density for different EOS. Diamonds correspond to the results of Ref. [40].

potential in pure neutron matter. Our calculations correspond to different choices of the interaction parameters. As can be seen from this figure the results are little dependent on the force parameters and are in good agreement with the results of Ref.[40], represented in diamonds.

In Fig. (5) is represented the neutron chemical potential as a function of the density in pure neutron matter. These calculations are also performed at zero temperature and for different values of Ω, for a fixed c value. The results of References [40], [49] and [50] are in diamonds, squares and dots, respectively. The calculations for the EOS with $\Omega = -100$ MeV are close to the SKM ones, those for the two other values of Ω show important differences at high density. Compared to the reference EOS at $\Omega = -100$ MeV, the results for $\Omega = -75$ MeV overestimate the neutron chemical potential at high density, while those for $\Omega = -125$ MeV underestimate it. These differences will affect the dynamical evolution.
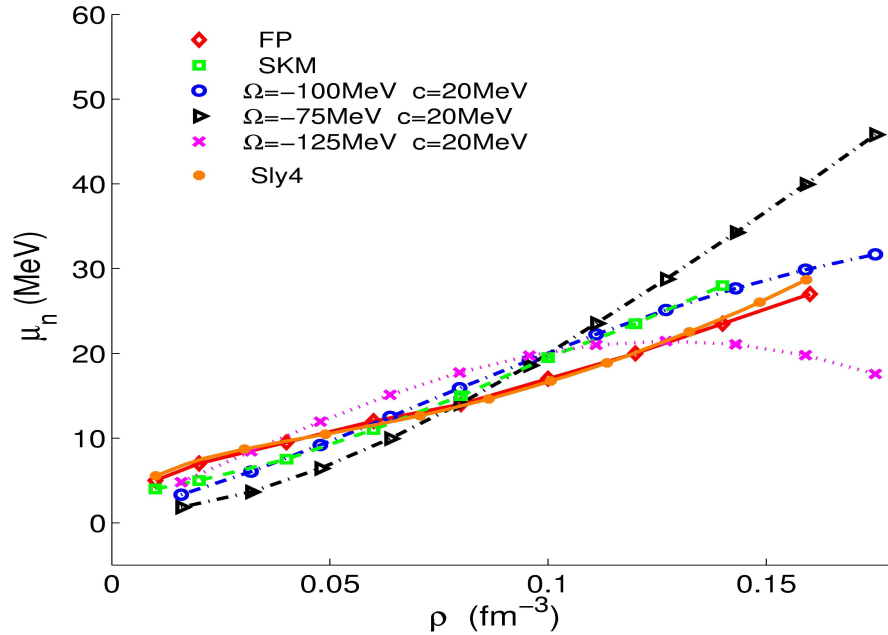
Figure 5: Neutron chemical potential in cold neutron matter as a function of the neutron density for different EOS. Diamonds, squares and dots correspond, respectively, to the results of Ref. [40], Ref. [49] and Ref. [50].

In the nuclear liquid drop model, the energy per baryon is written according to its expansion near saturation density as follows [41]:

$$\omega = \omega_0 + \frac{K_0}{18\rho_\infty^2}(\rho - \rho_\infty)^2 + [J + \frac{L}{3\rho_\infty}(\rho - \rho_\infty)]\delta^2 \tag{9}$$

where ω_0 and K_0 are, respectively, the coefficients related to the energy at the saturation density and the incompressibility modulus of symmetric nuclear matter. The coefficients J and L correspond, respectively, to the symmetry energy and to the density-dependent symmetry energy. If ρ_∞ and the two first coefficients are well determined by the experimental observations, the two last ones may have a wide region of uncertainty. In order to compare with other models, we give the relationships between different macroscopic properties of nuclear matter and the parameter set we used in the DYWAN modelization. According to Ref. [51] we have:

$$\omega_\delta = \frac{1}{2}\lim_{\delta \to 0}\frac{\partial^2\omega}{\partial\delta^2} \tag{10}$$

$$J = \omega_\delta(\rho_\infty) \tag{11}$$

13

$$L = 3\rho \frac{\partial \omega_\delta}{\partial \rho} \bigg|_{\rho=\rho_\infty} \tag{12}$$

$$K_{sym} = 9\rho^2 \frac{\partial^2 \omega_\delta}{\partial \rho^2} \bigg|_{\rho=\rho_\infty} \tag{13}$$

where K_{sym} represents the incompressibility of asymmetric nuclear matter, therefore it is related to K_0 by: $K_0 = K_{sym}(\delta = 0)$, and can also have a wide region of uncertainty. These definitions give the following relationship between the parameters Ω, c and L:

$$L = 6c + \Omega + L_{kin} \tag{14}$$

In Eq. (14) L_{kin} is the contribution of the kinetic energy density to L. From Fig. 2, when Ω increases (or equivalently, L) the energy of pure neutron matter decreases at low density (gas phase) and increases at high density (liquid phase). This behaviour may have an effect on the structures occurring in the simulations, as will be discussed later on in this paper.

In Fig. 6 we have plotted the values of L and of K_{sym} as a function of J. The squares A, B and C are the results of the DYWAN model for Ω= -75, -100 and -120 MeV, respectively. The remaining symbols are extracted from Skyrme Hartree-Fock (SHF) calculations from Ref. [51] and references therein. In this picture the equations of state A and B are close to the reference theoretical models, while the soft one C is too low for both quantities. We recall that we implemented here a simple effective force, with a small number of parameters, thus providing efficient computational formulae. Nevertheless, in spite of the simplicity of the force, the global trends of the calculated physical quantities displayed in this section are in good accordance with other theoretical approaches.

2.3 Dynamical evolution

At the reference level of our description, the dynamical evolution of the crystalline structure simulating the baryonic matter in a neutron star is given by a TDHF treatment of the supercell. At the densities and excitation energies involved in the star crust the mean free path of a single nucleon in nuclear matter remains relatively long [52, 53, 54]. In this case the dominant processes are two-body interactions in which small scale microscopic aspects, concerning quark and mesonic degrees of freedom, are averaged into the phenomenological self-consistent potential.
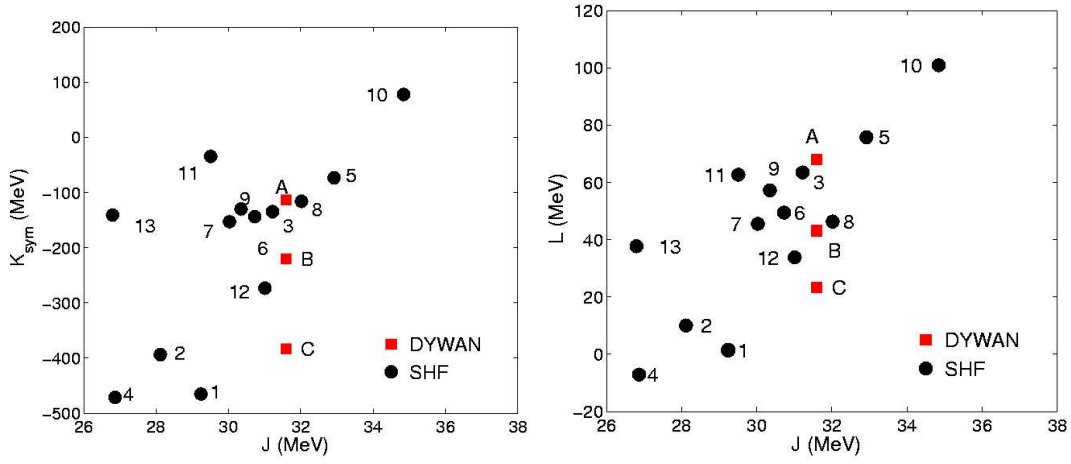
Figure 6: Correlations between macroscopic properties of asymmetric nuclear matter K_{sym} vs J (right) and L vs J (left). Full dots are Skyrme Hartree-Fock (SHF) calculations form Ref. [51] and squares are DYWAN results with Ω= -75 MeV (A), -100 MeV (B) and -120 MeV (C). The numbers denote the different parameter sets for SHF:1 for SI, 2 for SIII, 3 for SIV, 4 for SVI, 5 for Skya, 6 for SkM, 7 for SkM*, 8 for SLy4, 9 for MSkA, 10 for SkI3, 11 for SkI4, 12 for SkX, 13 for SGII.

The TDHF equations can been derived by different formalisms, in particular, from a time-dependent variational principle [55] based on the stationarity of the action:

$$\mathcal{S} = \int dt \ < \Psi|i\hbar\frac{\partial}{\partial t} - h|\Psi >$$

Here $< \Psi|i\hbar\frac{\partial}{\partial t} - h|\Psi >$ is the Lagrangian and $|\Psi >$ is the complete N-body wave function. The assumption here is that $|\Psi >$ is a Slater determinant of the s.p. wave functions $|\varphi_n >$ and h a one-body Hamiltonian in which the potential is the density-dependent effective interaction V^{HF}. In our model the s.p. wave-functions are projected on a discrete basis in Hilbert space :

$$|\varphi_\lambda > (t) = \sum_i c_i^\lambda |\alpha_i^\lambda > (t)$$

where the wave functions $\alpha_i^\lambda(x,t)$ are governed by time-dependent parameters and the c_i^λ are constant coefficients at zero temperature, determined by the initial conditions:

$$|\varphi_\lambda(0) >= |\varphi_\lambda^s >$$

The $|\varphi_\lambda^s >$ are the solutions of the stationary case (which is a particular solution of the TDHF equations). In this Lagrangian representation, it is straightforward to

show [28] that the elements of the moving basis evolve according to the following equations:

$$i\hbar\frac{\mathrm{d}}{\mathrm{d}t}|\alpha> = h(\rho)|\alpha> \tag{15}$$

Owing to the wave function decomposition, from the variational principle we obtain a system of coupled differential equations for the first and second moments in phase space coordinates:

$$\dot{\xi} = \frac{\pi}{m} + \frac{\partial}{\partial\pi}\mathcal{V} \tag{16}$$

$$\dot{\pi} = -\frac{\partial}{\partial\xi}\mathcal{V} \tag{17}$$

$$\frac{d\chi}{dt} = \frac{4\gamma\chi}{m} - \frac{\partial\mathcal{V}}{\partial\gamma} \tag{18}$$

$$\frac{d\gamma}{dt} = \frac{\hbar^2}{8m\chi^2} - \frac{2\gamma^2}{m} - \frac{\partial}{\partial\chi}\mathcal{V} \tag{19}$$

with the phase space correlation accounted for:

$$\gamma = \frac{\sigma}{2\chi} \tag{20}$$

and with the wavelet transform of the effective nuclear potential:

$$\mathcal{V} = <\alpha|V^{HF}|\alpha> \tag{21}$$

In consequence, equations (16)-(19), which are Hamilton type equations for the centroids and widths of the moving basis, solve the TDHF equations for the s.p. wave-functions. This result can be obtained in general in the framework of generalized coherent states theory [56].

Let us remark that in Eq. (21) the self-consistent mean-field is a function of the density extended to the overall supercell and not to a single WS cell. Then, as wavelets evolve in position and widths, they are able to interact with other wavelets belonging to different WS cells. Even more, the supercell is sensitive to its neighbours according to the periodic constraints since the wave function can freely spread and contribute to multiple super-cells, which are replicas of the central supercell . This is underlined in Fig. 7 where the density profile corresponding to a initial lattice of oxygen nuclei is represented as the function of time. The supercell is drawn in full line, it is built with 27 WS cells, each one containing one single nucleus. The system has been initially perturbed by introducing a slight variation on nuclei positions, and then released to evolve under the influence of the mean-field.
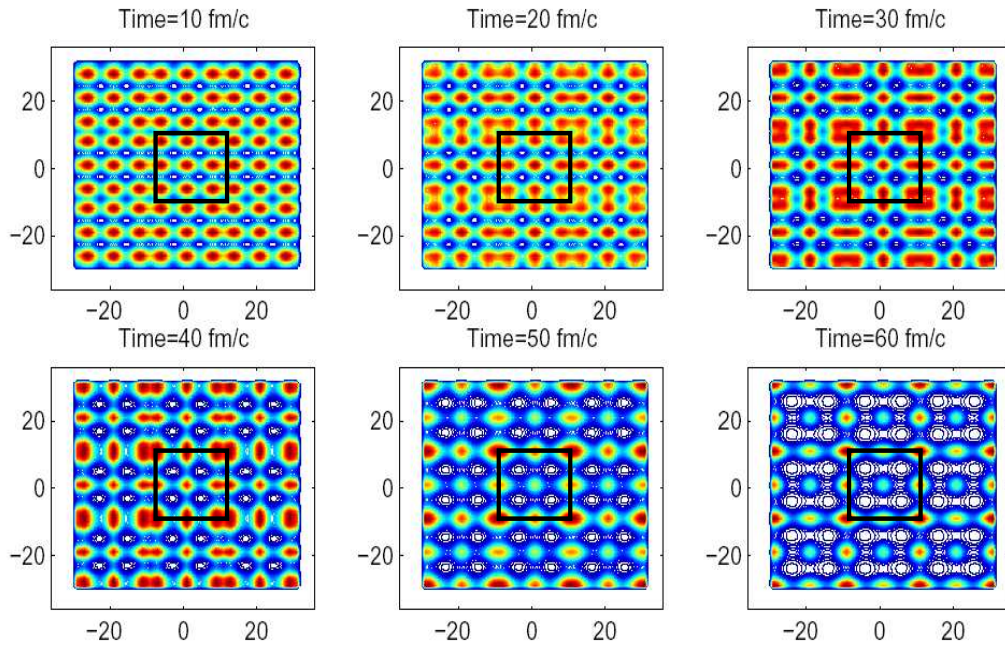
Figure 7: Time evolution of the two-dimensional density starting from an initial oxygen cubic lattice, in which the position of nuclei have been slightly shifted with respect their equilibrium positions.

3 Numerical treatment of the Coulomb interaction

The electron and nuclei Coulomb energies are important ingredients in the lattice global energy, with crucial consequences for the equilibrium sizes and shapes of nuclear matter in the inner crust. In our description periodic boundary conditions have been employed and the calculation of long range interactions as the Coulomb force requires a special care. The Ewald summation has been introduced [57] as a technique to sum efficiently the long-range interactions between particles and all their infinite periodic images. The basic idea of this method is to recast the Coulomb potential V^C, into two convenient terms which can be calculated in a fast and efficient way.

Taking into account the expansion of the density in terms of the Gabor coherent states (6), the Coulomb potential can be written as:

$$V^C(\vec{r}) = \sum_i \beta_i < v^c >_i (\vec{r}) + V_{el} \tag{22}$$

where V_{el} is the constant potential in space due to electrons and $< v^c >_i$ the contribution to the Coulomb potential due to an isotropic proton Gaussian state i:

$$< v^c >_i (\vec{r}) = \frac{q_i}{4\pi\varepsilon_0} \int \mathrm{d}^3r' \frac{g_{\bar{\chi}_i}(\vec{r'} - \vec{\xi}_i)}{|\vec{r} - \vec{r'}|} \tag{23}$$

Here $g_{\chi_i}(\vec{r})$ has the following form:

$$g_{\chi_i}(\vec{r} - \vec{\xi}_i) = \frac{1}{(2\pi\chi_i)^{3/2}} e^{-\frac{(\vec{r} - \vec{\xi}_i)^2}{2\chi_i}}$$

Following Ewald's method, the potential generated by a single charge is accounted for by the superposition of two contributions, on one hand the potential of the initial charge distribution complemented by a screening Gaussian charge distribution of equal magnitude and opposite sign, and on the other hand the potential of the screen with the same sign as the initial charge (Fig. 8).
According to this decomposition Eq. (22) can be written as the sum of two terms $V_d(\vec{r})$ and $V_r(\vec{r})$, which take into account, respectively, the short and the long range contributions. The short range contribution due to the screened charges is given in position space by:

$$V_d(\vec{r}) = \frac{1}{4\pi\varepsilon_0} \sum_j \frac{q_j}{|\vec{r} - \vec{r}_j|} \{\mathrm{erf}\,(\frac{|\vec{r} - \vec{r}_j|}{\sqrt{2\chi_j}}) - \mathrm{erf}\,(\frac{|\vec{r} - \vec{r}_j|}{\sqrt{2\chi'}})\} \tag{24}$$

Here χ' is the width of isotropic Gaussian screening functions with charge $-q_j$ and erf is the error function. On the other side $V_r(\vec{r})$ is the potential generated by both
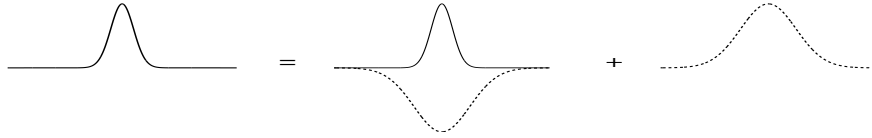
Figure 8: Components of a single charge contribution to the overall Coulomb potential, in full line the charge itself, in dotted line the screening charge.

the electron and the positive screening Gaussian distributions, which is calculated in momentum space by solving numerically the corresponding Poisson equation:

$$\Delta V_r(\vec{r}) = \frac{-1}{\varepsilon_0}(\rho_{screen}(\vec{r}) + \rho_{el}(\vec{r})) \tag{25}$$

From a computational point of view we have solved Eq. (25) on a grid using fast Fourier transforms techniques. In the above decomposition, the long range contributions of the direct term vanish and only the screened charges inside the supercell effectively contribute. In the external cells the potential is given by the reciprocal term, which is periodic. The choice of the width χ' permits to optimize the convergence of both V_d and V_r and at the same time to control the precision of the method since the overall potential must be independent of this parameter. The Ewald summation technique is widely investigated by different authors, for a recent review of these works we refer the reader to Ref. [58].

4 Morphological analysis of structural phases

In this section we give a brief description of a general method to characterize the morphology of two- and three-dimensional structures, which is based on concepts of integral geometry [59] developed in image analysis techniques. In the integral-geometry morphological image analysis (MIA) [60] numerical functions, called image functionals, assign numbers to the shape and connectivity of image patterns. The number of different functionals is equal to the dimension of the pattern plus one. In two or three dimensions these functionals are called Minkowski functionals and represent the surface, the mean convexity, the volume and the connectivity or Euler characteristics of the image. The last one is defined as:

$$\chi_E = n_e - n_t + n_c$$

where n_e is the number of elements, n_t the number of tunnels and n_c the number of cavities. We remark that this quantity is not normalized and depends on the size of

the lattice. In order to implement these functionals we map our density distributions onto a collection of black-and-white picture elements. We assign a black pixel to every point of the grid where the density is higher than a threshold value ρ_t. The variation of ρ_t allows to study different phases of the system.

Some of the basic structures occurring in our simulation are depicted in Fig. 9. We have also included on it the corresponding value of χ_E. It can be noticed that this quantity alone does not defines unambiguously the structures. In general one needs to give in addition another functional value, as for instance the mean convexity, which is always negative for bubble-like patterns. Table 2 summarizes the elementary structures we can obtain, and their corresponding Euler characteristic, according to a convenient choice of ρ_t.
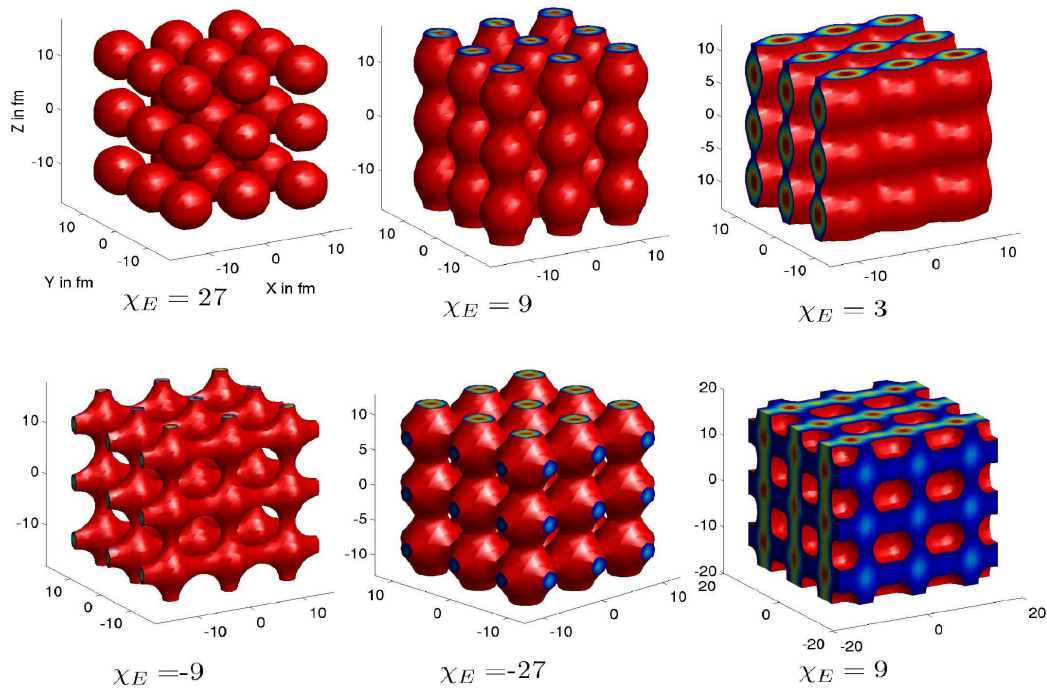

Figure 9: Various structural phases and their corresponding Euler characteristics.

5   Dynamical transitions of structural phases

In this section we show some results in the framework of the DYWAN model described in Sec. 2. Firstly, as an illustrative example, we have considered an initial cubic lattice of size L=24.6 fm, composed of 27 oxygen isotopes, with a proton fraction x=0.1 and at zero temperature. The resulting neutron distribution is plotted

Table 2: Summary of Euler characteristic values.

χ_E	structure
27	spheres
9	rods/spherical bubbles
3	slabs
-3	cylindrical bubbles
-9	slabs with holes
-15	connected slabs
-27	sponge

in Fig. 10 where the corresponding isodensity surfaces are represented as a function of time for the supercell. In this picture the threshold density is ρ_t=0.065 fm^{-3} while the average density is $< \rho >$=0.0725 fm^{-3}. This cell is of the same type as that of Fig. 7 but with a different initial condition in which nuclei are slightly deformed. In this case, starting from a lattice of nuclei under a quadrupole deformation, the system evolves passing through different structures, and remains rather stable, oscillating between different arrangements which keep a memory of the initial configuration. In Figures 7 and 10 we stress on the fact that meta-stable equilibrium states can be attained dynamically by the system in a pure mean-field evolution. In the example of Fig. 7 one observes that a very small variation of the initial position of some clusters in the lattice induces a reorganization of matter favouring the formation of heavier nuclei with different atomic number, as expected in realistic neutron star crusts.

We observe from this picture that in addition to (quasi) spherical nuclei, are produced phases with rod-like and slab-like nuclei, slabs with holes and bubbles. This result shows that the exotic phases are built dynamically from the initial lattice. The mechanical energy initially deposited in the lattice clusters permits the system to surf over different energy minima of similar values, without being trapped in one of them. Let us emphasize the fact that the numerical accuracy achieved in this framework is able to preserve the initial symmetries all along the dynamics, whose characteristic time duration are greater than 1000 fm/c. Therefore, one expects that relevant future investigations of dissipative as well as fluctuating effects will be performed without interfering with numerical defects or seeds.
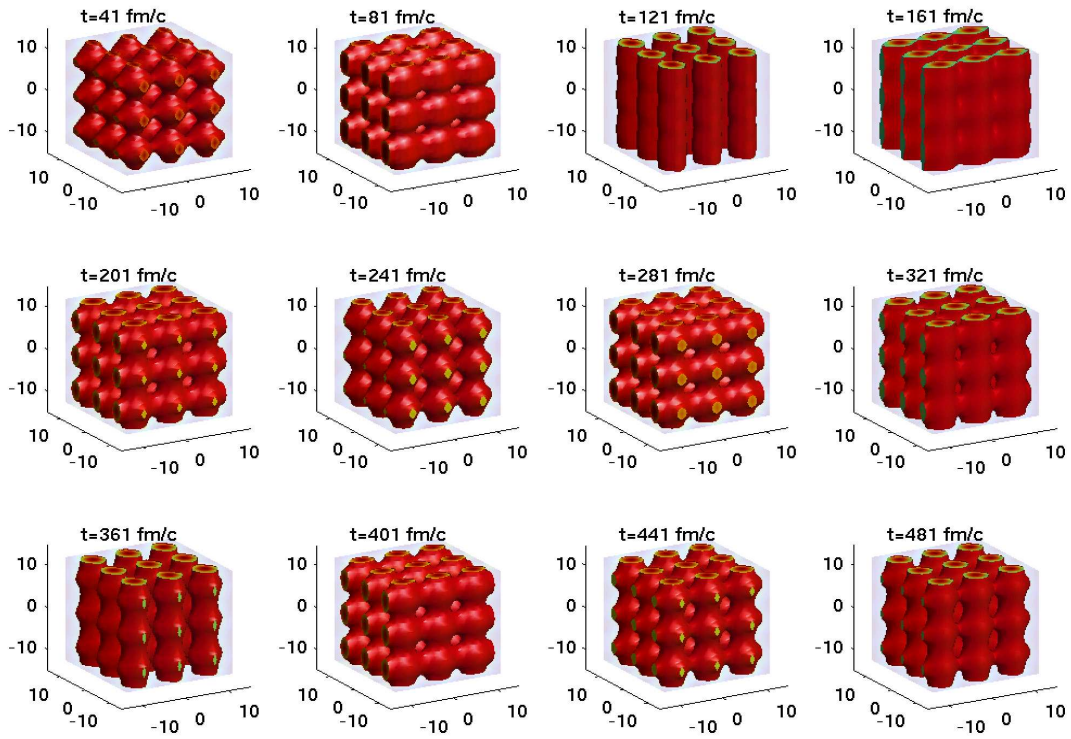
Figure 10: Time evolution of the neutron density for the 0.065 fm^{-3} threshold density corresponding to a proton fraction x=0.1 and mean density $< \rho >$=0.0725 fm^{-3}.

In order to characterize the preceding structures we have calculated the corresponding Euler characteristics as a function of time. In Fig. 11 are plotted $\chi_E(t)$ values versus t corresponding to the dynamical evolution in Fig. 10. According
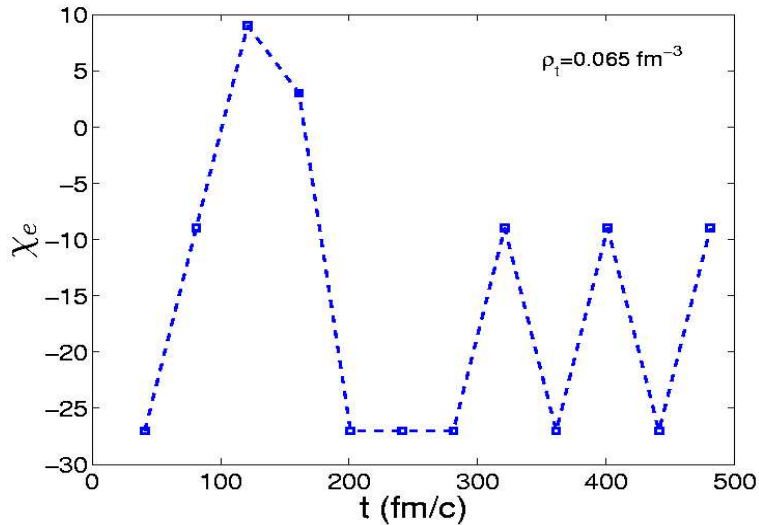

Figure 11: Euler characteristics as a function of time for the structures of Fig. 10

to Table 2 the system passes successively through sponge-like, slabs (with holes), rods, slabs and back to sponge-like phases, after which it oscillates between slabs and sponge phases. These results are strongly dependent on the threshold density ρ_t. Indeed, if for a given time we consider different values of this quantity, different structures are shown to appear. As a matter of example, we can consider the same system of Fig. 10 at t=201 fm/c, which corresponds to a sponge-like structure for the threshold density ρ_t=0.065 fm^{-3}. In this case, as shown in Fig. 12 for a density ρ_t=0.09 fm^{-3} the structure corresponds to an arrangement of spherical nuclei, while for ρ_t=0.05 fm^{-3} to cylindrical bubbles.

The previous discussions indicate that the formation of non-spherical phases and the transitions between them are processes of dynamical nature, in accordance with the suggestion of Ref. [27], where the same aspect has been observed despite different initial configurations. Even more, different morphological structures corresponding to different threshold densities can exist at a given time and for a given average density. The occurrence of these embedded structures makes their characterization not trivial. In order to get a better understanding about the interplay between the different physical quantities entering in the dynamics we extracted the asymptotic Euler characteristics corresponding to different bins of the threshold density, for a
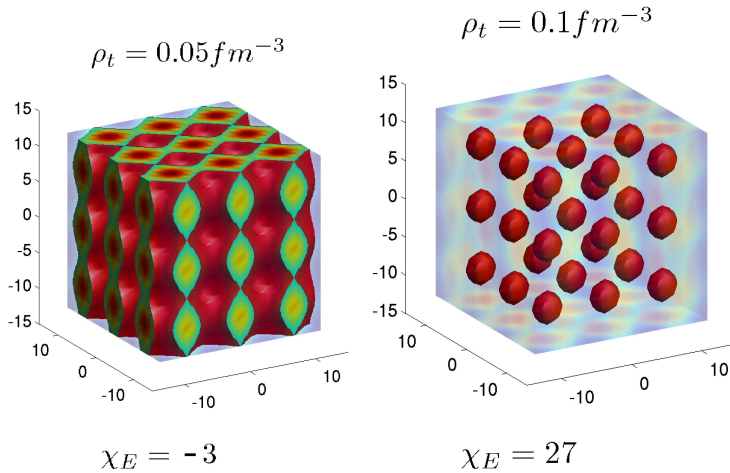
Figure 12: Neutron density for the same system as in Fig. 10 at t=201 fm/c for two values of the threshold denstity ρ_t.

variety of systems characterized by their mean densities and proton fractions.

Typical plots for the neutron distributions of density threshold ρ_t versus the nucleon average density $< \rho >$ are represented in Fig. 13 where the different zones correspond to well defined structures (or χ_E values). For simplicity's sake, we have considered a coarse-grained classification of phases: spherical (black), cylindrical (light grey), planar (dark grey), sponge-like structures (white) and bubbles (grey). In these calculations we have implemented three versions of the asymmetry parameter Ω in order to analyze the sensitivity of the results to the EOS, while keeping fixed the other parameters of the force.

As before, we observe in these pictures that for a fixed mean density different structures are present. Conversely, for a given value of threshold density ρ_t and for growing values of the average density the system takes successively different structures. For x=0.2 (on the left) the system passes through all the above mentioned structures, in that order. This behaviour follows the typical picture of phases sorting suggested by the pioneer works of Ref. [6, 7] and with recent works, where the authors of Ref. [10, 44] found complex structures like the sponge-like ones, which they called "intermediate" phases. The phase diagrams in these works are given in a one dimension representation. Our structure diagrams being two-dimensional plots, in Fig. 13 equivalent structures can be observed along the density axis, for a bin in

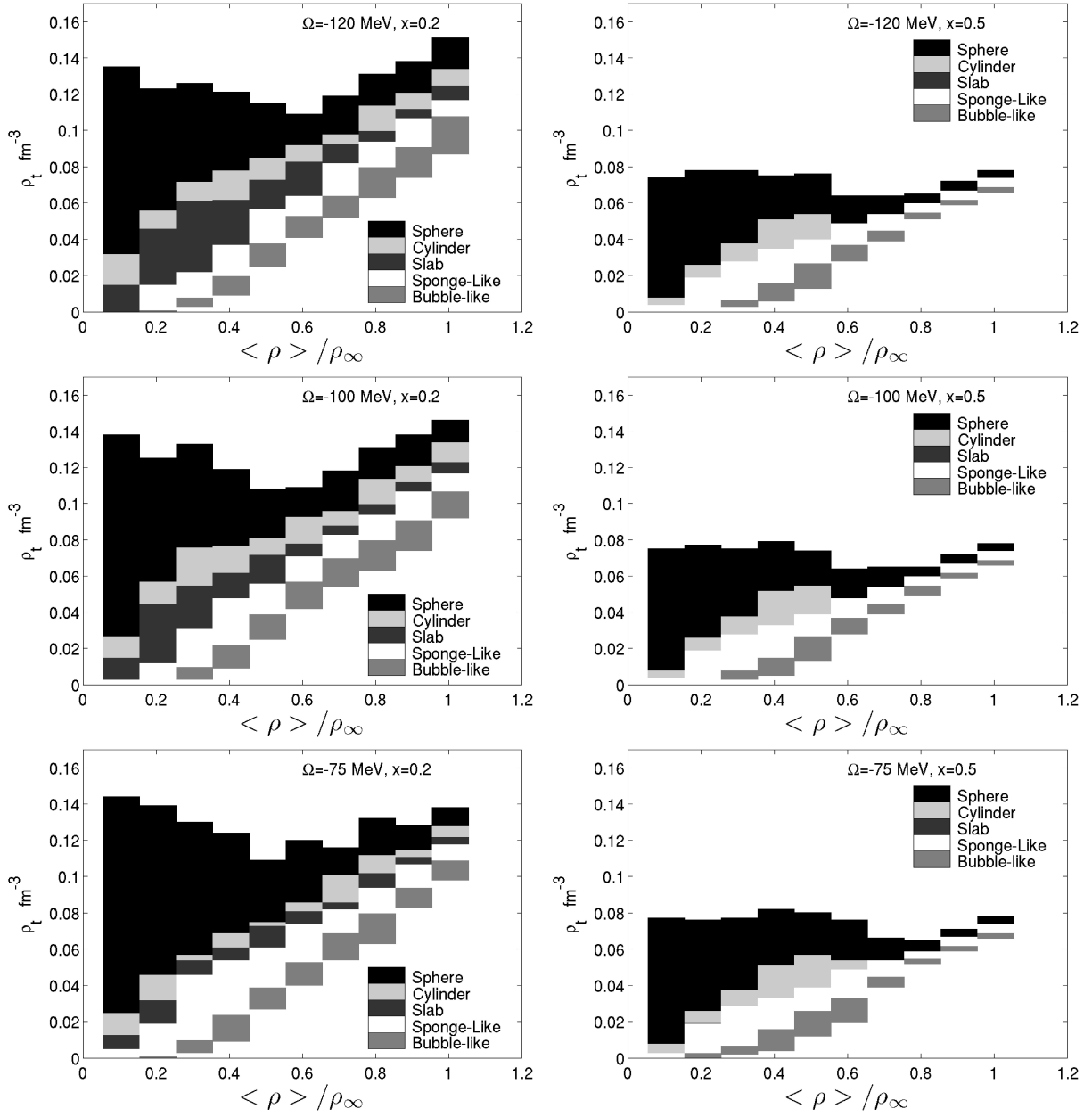Figure 13: Neutron threshold density versus the neutron mean density normalized to the saturation value for different values of Ω and for two proton fractions : x=0.2 (left) and x=0.5 (right). The different structures are in grey scales.

25

the threshold density of around 0.05 fm^{-3}.

Let us first address the case of symmetric matter (on the right). A global observation can be done, the structure diagram is weakly dependent on the EOS. With a proton fraction x=0.5 neutron and proton distribution functions may differ locally, in particular, due to the Coulomb interaction. Nevertheless, the isospin fingerprints of the effective force for this proton fraction are washed out. In any case there is not formation of slabs, we just observe a slight increase of the rod structure region with $\Omega = -75$ MeV, which is the "stiff" force with respect to the isospin asymmetry.

In the case of proton fraction x=0.2 (on the left) the structure diagram is different, indeed more distinct structures can exist at low mean densities and more complex structures appear on a larger region of neutron threshold densities. It must also be kept in mind that we are not dealing with homogenous matter, the system can freely self-organize inside the supercell, therefore locally the nucleon density can strongly differ from the average one. This is specially expected with strong isospin asymmetries (low proton fractions) owing to the fact that the proton chemical potential becomes strongly negative along with increasing positive neutron chemical potential. In this case the influence of the EOS is more perceptible. Indeed, one observes that as the force softens (for increasing Ω values), the region concerning the slab formation increases and the one corresponding to sponge-like phases decreases. The region with bubbles tends also to decrease with increasing Ω for the higher average densities.

A qualitative interpretation of the conspicuous EOS fingerprints on the structure diagram is provided by the sensitivity of neutron chemical potential to the isospin stiffness. According to Fig. 5, the density variation of the neutron chemical potential in pure neutron matter is stronger for the stiffest effective interaction. Therefore, the emission of neutrons located near the surface will be favoured, or equivalently, the probability that neutron wave functions spread in all directions will increase. This is emphasized by a clear increase of sponge-like structures, in correlation with a greater spatial extension of the neutron liquid, linking the residual clusters. For this reason, the minimum threshold density for the onset of spherical structures is lowered.

In Fig. 14 we have displayed neutron (top) and proton (bottom) two-dimensional density distributions for two proton fractions: $x = 0.5$ (right) and $x = 0.2$ (left). We considered the effective force with the standard value of Ω= -100 MeV. In symmet-
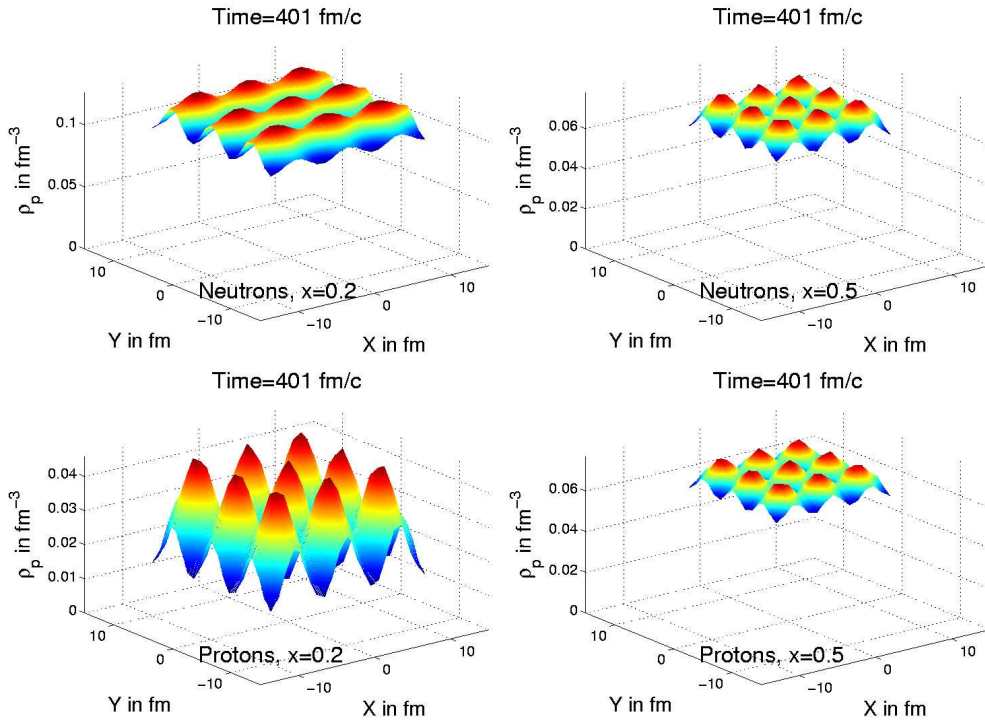
Figure 14: Density distributions of neutrons (top) and of protons (bottom) at t=401 fm/c in the plane $z = 0$, for two values of the proton fraction : $x = 0.2$ (left), $x = 0.5$ (right) and with Ω=-100 MeV.

ric matter neutron and proton profiles have similar shapes involving small density variations. For asymmetric matter ($x = 0.2$) protons are localized inside cluster structures. These results can be put in parallel with Figs. 4 and 5 where proton and neutron chemical potentials in pure neutron matter (respectively μ_p and μ_n) are displayed as a function of the average density. We observe that the minima of μ_p are at high density, whereas μ_n experiences its minima for the lowest densities. Consequently, a neutron excess in high density spots leads to emission processes towards vacuum regions, with a correlated inhibition of the proton emission. Finally, considering the energy density per baryon (Fig. 3), one also observes a strong sensitivity to the proton fraction at high nucleon density, which compels the protons to remain in cluster structures while delocalizes neutrons contributing to build the neutron gas.

6   Conclusions

In this article we have presented a dynamical investigation of the outermost layer in neutron stars. The foundations of the dynamical description are based on the DY-WAN approach of heavy-ion collisions, which has been successfully confronted with experimental data [29, 30]. In this framework, the stellar crust is self-consistently determined starting from an infinite periodic crystal of nuclei immersed in a degenerate electron gas. The principal static properties of nuclear matter have been compared with other theoretical calculations. Despite the implementation of a simplified effective force, the main nuclear properties like energy densities and chemical potentials are shown to be in close agreement with the commonly accepted theoretical trends. In the current version of the model the evolution of the system is ruled by the nuclear mean-field, owing to the fact that we focus the investigation on the crust matter at zero temperature .

A variety of structural phases, the so-called "pasta phases", are shown to be built self-consistently from the microscopic nuclear motion. The morphology of these structures has been analyzed using integral geometry techniques, revealing their complexity. Beyond spherical nuclei, rod-like, slabs, cylindrical bubbles, slabs with holes, connected slabs and sponges have been found. These phases are formed dynamically allowing the transitions between different kind of structures having ground state energies close to each others.

We have also evidenced that, at variance with common macroscopic interpre-

tations, the spreadings of the wave functions induce the imbrications of different geometrical structures each one appearing for well defined bins of the threshold density ρ_t. Structure diagrams in the plane defined by ρ_t and the overall mean density $< \rho >$ have been plotted for two proton fractions (0.2 and 0.5) and different versions of the force at asymptotic times. A clear sensitivity to the EOS has been evidenced for the low proton fraction, while in symmetric nuclear matter the results are almost independent of it. These plots exhibit a conspicuous increase of the regions of spherical and sponge-like structures against those of slabs and cylinders as the effective force is stiffer. In this case, the neutrons are dripped preferentially in three-dimensional geometries rather than in linear or in planar structures.

The energy level densities of bound particles depend on the effective interaction. It will therefore be possible to investigate in this framework the influence of different aspects as the non-locality of the force and shell effects. This investigation will provide the opportunity to probe the different dynamical paths of the system on a complex energy manifold and to analyze the lattice fingerprints on different phases as well as the existence of various lattice geometries. A special attention has been devoted to the numerical treatment in order to avoid unphysical symmetries breaking due to uncontrolled numerical fluctuations. The good dynamical response to initial excitations is evidenced by the fact that symmetries are preserved during long time intervals in the current simulations. The problem of handling unwanted numerical errors is crucial in order to tackle afterwards the study of physical correlations and fluctuations. The study of hot and excited matter behaviour, dissipation as well as fluctuation effects will therefore be reachable in this context.

References

[1] W. Baade and F. Zwicky, Phys. Rev. **46** (1934) 76.

[2] M. Herant, W. Benz, W.R. Hix, C. Fryer and S.A. Colgate, Astrophys. J. **435** (1994) 339, A. Burrows; J.Hayes and B.A. Fryxell, Astrophys. J. **450** (1995) 830; W. Hillebrandt and J.C. Niemeyer, Ann. Rev. Astron. Astrophys. **38** (2000) 191 and references therein, G. Martínez-Pinedo, M. Liebendörfer, D. Frekers, Nucl. Phys. A **777** (2006) 395.

[3] C.J. Pethick and D.G. Ravenhall, Annu. Rev. Part. Sci. **45** (1995) 429.

[4] A. Burrows and J.M. Lattimer, Astrophys. J. 307 (1986) 178.

[5] P. Haensel, A.Y. Pothekin and D.G. Yakovlev, Neutron Stars 1: Equation of State and Structure, Springer (2007).

[6] D.G. Ravenhall, C.J. Pethick, and J.R. Wilson, Phys. Rev. Lett. **50** (1983) 2066.

[7] M. Hashimoto, H. Seki and M. Yamada, Prog. Theor. Phys. **71** (1984) 320.

[8] P. Napolitani, P. Chomaz, F. Gulminelli and K.Hasnaoui, Phys. Rev. Lett. 98 (2007) 131102.

[9] P. Chomaz, F. Gulminelli, C. Ducoin, P. Napolitani and K. Hasnaoui, Phys. Rev. C 75 (2007) 065805.

[10] G. Watanabe et al. Phys. Rev. C **66** (2002) 012801(R).

[11] C.J. Horowitz, M.A. Pérez-Garcia and J. Pieckarewicz, Phys. Rev. C **69** (2004) 045804.

[12] R.D. Williams and S.E Kooning, Nucl. Phys. A **435** (1985) 844.

[13] M. Lassaut, H. Flocard, P. Bonche, P.H Heenen and E. Suraud, Astro. Astrophys. **6** (1987) 183.

[14] K. Oyamatsu, Nucl. Phys. A **561** (1993) 431.

[15] M. Onsi, A.K. Dutta, H. Chatri, S. Goriely, N. Chamel and J.M. Pearson, Phys. Rev. C **77** (2008) 065805.

[16] C.P. Lorenz, D.G. Ravenhall and C.J. Pethick, Phys. Rev. Lett. **70** (1993) 379.

[17] F. Douchin and P. Haensel, Phys. Lett. B **485** (2000) 107.

[18] G. Watanabe, K. Iida and K. Sato, Nucl. Phys. A **676** (2000) 455.

[19] T. Maruyama, K. Niita ,K. oyamatsu, T. Maruyama, S. Chiba and A. Iwamota, Phys.Rev. C **57** (1998) 657.

[20] J.W. Negele and D. Vautherin, Nucl. Phys. A **207** (1973) 298.

[21] P. Magierski and P.-H.Heenen, Phys. Rev. C **65** 045804 (2001) 461.

[22] P. Magierski, A. Bulgac and P.-H.Heenen, Nucl. Phys. A **719** (2003) 719.

[23] M. Baldo, C. Maieron, P. Schuck and X. Viñas, Nucl. Phys. A **736** (2004) 241.

[24] F. Montani, C. May and H Muther, Phys.Rev. C **69** (2004) 0645801.

[25] P. Gogëlein, E.N.E. van Dalen, C. Fuchs and H. Müther, Phys. Rev. C **77** (2008) 025802; J.M. Pearson,Phys. Rev. C **77** (2008) 025802.

[26] T. Bürvenich, I.N. Mishustin and W. Greiner, Phys.Rev. C **76** (2007) 034310; K.S. Cheng, C.C. Yao and Z.G. Dai, Phys. Rev. C **55** (1997) 2092.

[27] G. Watanabe, T. Maruyama, K. Sato, K. Yasuoka and T. Ebisuzaki, Phys. Rev Lett. **94** (2005) 031101.

[28] B. Jouault, F. Sébille and V. de la Mota, Nucl. Phys. A **628** (1998) 119.

[29] F. Sébille et al., Nucl. Phys. A **756** (2005) 229; *ibid* Nucl. Phys. A **791** (2007) 313; *ibid* Phys. Rev. C **76** (2007) 024603.

[30] V. de la Mota and F. Sébille, Eur. Phys. Jour.A **12** (2001) 479.

[31] R. Balian,Y. Alhassid and H. Reinhardt, Phys. Rep. **131** (1986) 1; J. Rau and B. Müller, Phys Rep **272** (1996)1.

[32] B. Carter, N. Chamel, P. Haensel, Nucl. Phys. A **748** (2005) 675.

[33] T. Maruyama, T. Tatsumi, D.N. Voskresensky, T. Tanigawa, and S. Chiba, Phys. Rev. C **72** (2005) 015802; G. Watanabe and K. Iida, Phys. Rev. C **68** (2003) 045801.

[34] N. Chamel, S.Naimi, E.Khan, and J.Margueron, Phys. Rev. C **75** (2007) 055806.

[35] N. Chamel ,Nucl. Phys. A **747** (2005) 109.

[36] L. Zamick, Phys. Lett. B **45** (1973) 313.

[37] D. Idier et al. Ann. Phys. Fr.**19** (1994) 159.

[38] E. Chabanat, P. Bonche, P. Haensel, J. Meyer, R. Schaeffer, Nucl. Phys. A **635** (1998) 231.

[39] K. Oyamatsu and M. Yamada, Nucl. Phys. A **578** (1994) 181.

[40] B. Friedman, V.R. Pandharipande, Nucl. Phys. A **361** (1981) 501.

[41] K. Oyamatsu and K. Iida, Phys. Rev. C **75** (2007) 015801.

[42] M.Unser and A. Aldroubi, Polynomial splines and wavelets- A signal processing perspective in Wavelets: A tutorial in Theory, Ed. C.K. CHUI, Academic Press (1992) 91-122.

[43] A. M. Perelomov, Generalized coherent states and their applications (1986), Springer Verlag.

[44] G. Watanabe, K. Sato, K. Yasuoka, T. Ebisuzaki, Phys. Rev. C **68** (2003) 035806; *ibid* **69** (2004) 055805; H. Sonoda, G. Watanabe, K. Sato, T. Takiwaki, K. Yasuoka, T. Ebisuzaki, Phys. Rev. C **75** (2007) 042801(R).

[45] G. Baym, H.A. Bethe, C.J. Pethick, Nucl. Phys. A175 (1971) 225.

[46] J. Arponen Nucl. Phys. A **191** (1972) 257.

[47] H. Shen, H. Toki, K. Oyamatsu and K. Sumiyoshi, Nucl. Phys. A **637** (1998) 435-450.

[48] A. Akmal, V.R. Pandharipande and D.G. Ravenhall, Phys. Rev. C **58** (1998) 1804.

[49] H. Krivine, J. Treiner and O. Bohigas, Nucl. Phys. A **336** (1980) 155.; C.J. Pethick, D.G. Ravenhall and C.R Lorenz,Nucl. Phys. A **584** (1995) 675.

[50] F. Douchin, P. Haensel, Phys. Lett. B **435** (2000) 107.

[51] S. Yoshida and H. Sagawa, Phys. Rev. C **73** (2006) 044320.

[52] V.R. Pandharipande and S.C. Pieper, Phys.Rev. C **45** (1992) 791.

[53] F. Sammarruca , Phys.Rev. C **77** (2008) 047301.

[54] W. Zuo, G. Giansiracusa , U. Lombardo, N. Sandulescu and H.-J. Schulze, Phys.Lett. B **421** (1998) 1.

[55] A.K. Kerman and S.E. Koonin, Ann. Phys. **100** (1976) 332.

[56] E.J. Heller, J. Chem. Phys. **64** (1975) 1544; *ibid* **64** (1976) 62.

[57] P. Ewald, Ann Phys. **64** (1921) 253.

[58] A. Y. Toukmaji and J.A. Board, Tr. Comp. Phys. Comm. **95** (1996) 73.

[59] L.A. Santaló, Integral geometry and Geometric Probability, Addison-Wesley, Reading,MA (1976); D. Stoyan, W.S. Kendall and J. Mecke, Stochastic Geometry and its Applications, Akademie Verlag, Berlin (1989).

[60] K. Michielsen and H. De Raedt, Phys. Rep. **347** (2001) 461.